Feasibility Study of Using PEImager Scanner for Positron Emission Mammography

Meei-Ling Jan, *Member, IEEE*, Keh-Shih Chuang, Yu-Ching Ni, Cheng-Chih Pei, Jay Wu, Ching-Kai Yeh, and Ying-Kai Fu

***Abstract*—The purpose of this work is to study the feasibility of using a PEImager scanner in positron emission mammography (PEM). PEM was performed using two opposite block detectors of the PEImager without rotating). One projection image or several focal-plane images were obtained by dual-head imaging, because the number of line of response (LOR) to be reconstructed into tomograms by conventional sinogram-based reconstruction methods is limited. In this work, an iterative algebraic reconstruction was employed to reconstruct projection data to obtain a tomogram. The locations and sizes of hot spots in a breast phantom can be interpreted using such planar tomography, considering the efficiency of detector elements, attenuation and geometric factors. Spheres with diameters of 3 mm, 5 mm, 8 mm and 10 mm were inserted into a cylindrical phantom simulated tumors embedded in the background with different radioactivities, to evaluate the tumor detection capacity capability of tumor detection. For an 80-mm-depth phantom with a 20:1 tumor-to-normal tissue radioactivity ratio, a tumor with a diameter of 3 mm can be detected using planar tomography, while a 5-mm-diameter and 10-mm-diameter tumors can be detected in the ratios 10:1 and 5:1, respectively. The images of planar tomography have better contrast than focal-plane reconstruction, and have greater tumor-detection capacity ability.**

***Index Terms*—Breast imaging, PEM, positron emission mammography.**

I. Introduction

BREAST cancer remains a major cause of cancer deaths among women in many parts of the world. Early detection has been demonstrated to be the most effective strategy to reduce breast cancer mortality. Mammograms are today the most used means of diagnosing breast cancer. Mammography is inexpensive and readily available, but the low contrast resolution among soft tissues caused by the minor difference between the X-ray attenuations of normal and abnormal tissues cause mammography to suffer from the high percentage of false positives [1]. The alternative techniques, such as positron emission tomography have been developed to improve the sensitivity of the detection of small lesions. Several investigations have suggested that whole-body PET using the tracer F-18-fluorodeoxyglucose ([^{18}F]-FDG) provides excellent sensitivity ($\sim$90%) and specificity ($\sim$90%) for both malignant breast tumors and axillary node involvement [2]–[4]. The whole-body PET scanners are expensive and the large separation distances between the detectors limits the solid angle, the spatial resolution and the sensitivity, so a number of groups have proposed and built dedicated low-cost, high-resolution, high-sensitivity scanners for breast cancers [5]–[10]. These dedicated breast imaging devices, called positron emission mammography scanners, are especially designed with increased sensitivity for tumor detection.

In this study, a positron emission imager (PEImager) developed in the authors' laboratory was used as a PEM prototype. The designs for a breast imaging scanner were evaluated based upon two position-sensitive BGO detectors. The PEImager scanner consists four block detectors and with projection and tomographic imaging abilities [11]. Two opposite detectors were used to acquire data with no rotation to study the feasibility of applying the PEImager scanner for breast imaging. These projection data obtained from two-detector imaging provide less depth information, and the number of LORs to be reconstructed by conventional sinogram-based reconstruction is limited, so only one projection image or several focal-plane images were obtained [7], [9], [12], [13]. This study introduces the imaging system and the planar-tomography algorithm for reconstructing projection data. The spatial resolution of planar tomography was evaluated and compared with those of focal-plane and conventional tomography. Hot spots of various sizes at various locations in water were investigated to assess the performance of this prototype PEM scanner. This scanner has many fewer detectors than regular whole-ring PET scanners, so the cost is lower. Furthermore, the scanner can be adjusted to position the detectors as close as possible to the breast, to increase the detection sensitivity and reduce the injection dose. The imaging quality of this scanner may not be as good as that of a dedicated PET, and it has the potential to detect early breast cancers simply, effectively and inexpensively.

II. Material and Methods

A. System Description

The PEImager system (Fig. 1) developed at our laboratory is composed of four block detectors mounted on a rotating plate, which can rotate through 90° to achieve 360° data acquisition

Manuscript received January 18, 2004; revised November 24, 2004. This work was supported in part by the National Science Council, Taiwan under Grant NSC91-2623-7-007-008-NU.

M.-L. Jan is with the Institute of Nuclear Energy Research, Longtan 32546, Taiwan, R.O.C. and also with the Department of Nuclear Science, National Tsing-Hua University, Hsinchu 30043, Taiwan, R.O.C. (e-mail: mljan@iner.gov.tw).

K.-S. Chuang and J. Wu are with the Department of Nuclear Science, National Tsing-Hua University, Hsinchu 30013, Taiwan, R.O.C. (e-mail: kschuang@mx.nthu.edu.tw).

Y.-C. Ni, C.-K. Yeh, and Y.-K. Fu are with the Institute of Nuclear Energy Research, Longtan 32546, Taiwan, R.O.C.

C.-C. Pei was with the Institute of Nuclear Energy Research, Longtan 32546, Taiwan, R.O.C. He is now with the Department of Information Management, Wufeng Institute of Technology, Chiayi 62153, Taiwan, R.O.C..

Digital Object Identifier 10.1109/TNS.2005.858180

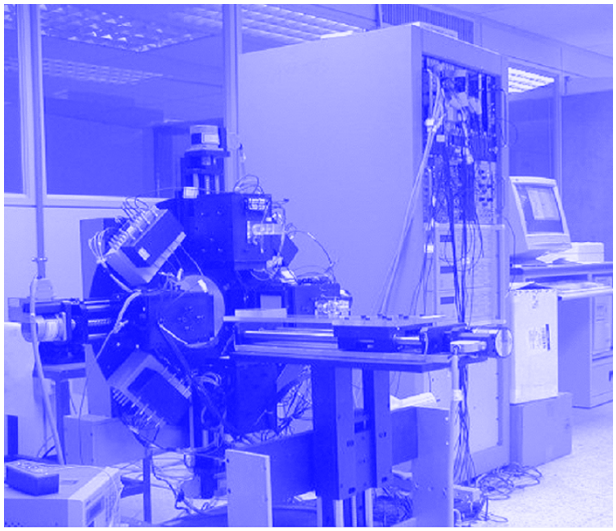

Fig. 1. Photograph of the PEImager system.

with a stepping motor. The geometric setup of the scanner is flexible and allows the center-detector distance to be adjusted in the range 110 mm to 190 mm, according to the sensitivity requirement and the size of the object to be scanned. Each block detector of the PEImager consists of an array of 18 × 16 small individual BGO scintillating crystals of dimensions $2.65\ \mathrm{mm} \times 2.65\ \mathrm{mm} \times 25\ \mathrm{mm}$. The center-to-center space of these crystals is 2.8 mm. The crystal matrix was coupled to a 76.2 mm × 76.2 mm Hamamatsu R3941-02 position-sensitive photomultiplier tube. The PEImager is a PC-based system that performs data acquisition, to control stepping motors, rotate the plate and move the couch. The readout analog signals from detectors are processed by the NIM (Nuclear Instrument Module) modules, and the digitalized signals are processed by the CAMAC (Computer Automated Measurement and Control) modules [14]. The PEImager has two imaging options to acquire data. When the data are collected using the planar imaging mode, two opposite detectors are effective and a two-dimensional planar projection image is obtained. If the tomographic imaging mode is chosen, four detectors are rotated through 90°, and a three-dimensional tomographic image is obtained.

During data acquisition, logical AND units are used to check the coincidence condition with a timing window of 20 ns. Coincident events for all energy window combinations and all LORs are collected in list-mode format. The processes are calculating the position; identifying crystal numbers using look-up tables (LUTs) of crystals; binning; rebinning and reconstruction. These are implemented with in-house software developed in C/C++ language. After the crystal and energy have been determined, all of the recorded events matched with energy window confinement were binned to two-dimensional projection images or three-dimensional sinograms, according to the choice of acquisition modes. For the stationary two-detector imaging mode of the PEImager, there are 82 944 LORs, and the maximum oblique angle of these LORs is 12.9°. In the past, the listed raw data were binned to an image with 35 ×31 pixels, which was then interpolated to 128 × 128 pixels. The field-of-view (FOV) of the projection image is 50.4 mm by 44.8 mm. In the tomographic imaging process, the listed three-dimensional data are binned to 256 sinograms, which consist of 4 976 640 LORs for 30 rotating angles. Subsequently, the correction for center-of-rotation calibration was performed. The acquired sinograms are reconstructed into 31 slices with 128 × 128 pixel per slice by filtered backprojection reconstruction. The pixel size is 0.39 mm in the transverse planes. This mode has a transaxial length of 50.4 mm and an axial length of 44.8 mm FOV. For tomographic imaging, the transaxial resolution full-width at half maximum (FWHM) is 2.73 mm (radial) and 2.99 mm (tangential) at the center [11]. For PEM studies, the third reconstruction—planar tomography is developed. The details are as follows.

B. Reconstruction Algorithm for Planar Tomography

For PEM studies, only two stationary detectors were employed in data acquisition. The detector-to-detector distance is large in relation to the area of the block detector, and the LORs in the sinograms have limited angular range, so conventional PET reconstruction algorithms are not used for this two-detector imaging [15], [16]. Most of the parallel plane PEM cameras used the focal-plane algorithm [7], [9], [12], [13] for reconstructing images. The primary shortcoming of this algorithm is that the activities occur in every plane, and form broad background radioactivity. Based on focal-plane reconstruction, an iterative method is implemented to reconstruct the image of the limited LORs. The list-mode data from the two typical detectors were firstly binned to a frame matrix with dimensions 288 × 288. The LORs from two parallel detectors were projected in tandem to the reconstruction volume. The number of the voxels in this study was set to $36 \times 32 \times 58$ with dimensions $1.4 \times 1.4 \times 1.4\ \mathrm{mm}^3$ for each voxel. Let f_i be the average radioactivity inside the i^{th} voxel of the unknown image; w_{ij} be the overlapping area between the i^{th} voxel and the j^{th} LOR; g_{ij} be the geometric efficiency of the i^{th} voxel to the detector pairs connected via the j^{th} LOR, and C_j and C'_j be the total number of measured and estimated detections, respectively, along the j^{th} LOR after efficiency of the detector pair has been corrected. Then

$$C'_j = \sum_i f_i w_{ij} g_{ij}. \tag{1}$$

The reconstruction begins with guessing an initial value of the universal constant for all voxels. The subsequent iteration is performed according to

$$f'_{ij} = \frac{C_j}{C'_j} w_{ij} g_{ij} f_i^{(k)}, \tag{2}$$

$$f_i^{(k+1)} = \frac{1}{\sum_j w_{ij} g_{ij}} \sum_j f'_{ij} \tag{3}$$

where f'_{ij} is the contribution from the j^{th} projection data to the i^{th} voxel, and C_j/C'_j is the discrepancy between the total number of measured and estimated detections, respectively, along the j^{th} LOR in the projection space. Notably, the normalization term $\sum_j w_{ij} g_{ij}$ compensates for the unequal geometric efficiency for sources at various locations.

In conventional focal-plane reconstruction, the focused plane determines the Z location of the radioactivity source [9], indicating that the plane that is most likely to be with radioactivity

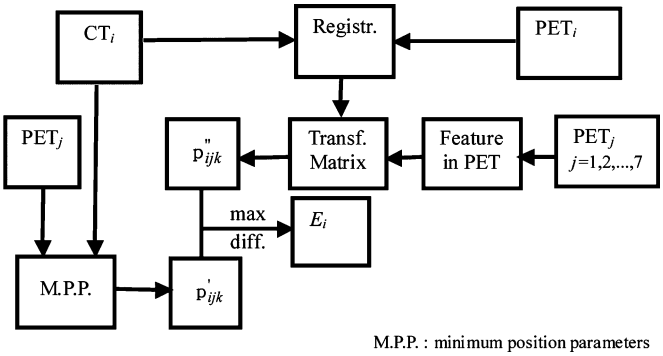

Fig. 2. Reconstruction flowchart of planar tomography.

has a higher "density" (counts per voxel) than the nonfocused plane. Based on this concept, the algorithm is further implemented by iteration, with the correction term proportional to the "density" of each voxel, and not simply obtained merely by dividing the measured ray-sum and the computed ray-sum uniformly over the length of the ray. That is, a voxel with a greater count will have a greater contribution from the projection data for each backprojection in the proposed reconstruction algorithm. Equations (2) and (3) reveal that the formula is similar to that of MLEM [17], [18], although the Poisson nature of data was not taken into account. A thresholding method is used to accelerate the iterative reconstruction. After each iteration, if the radioactivity of a voxel is smaller than a threshold value [19] δ, then this value is taken as noise and is then set to zero

$$f_i^{(k+1)} = 0, \quad \text{if} \quad f_i^{(k+1)} < \delta. \tag{4}$$

Fig. 2 presents a flow chart of the reconstruction algorithm.

C. Calibrating Efficiency of the Detector

An F-18-fluid flood source was measured to calibrate the efficiency of the detector based on the crystal level. The source was placed in the center between two opposite, parallel detectors. The total counts detected along a LOR depend on the geometry and detector efficiency. The geometry factor of each LOR was calculated in advance according to the solid angle of the uniform radioactivity source and detector-element pair. After the geometry factor was calibrated, the detector efficiency response was assumed to be the only factor that influences the uniformity of the counts that are summed to a LOR.

D. Spatial Resolution

Spatial resolutions of the focal-plane, planar tomography and tomography were evaluated using a line source in air. The source holder was a needle with an internal diameter of 0.6 mm, and was filled with ^{18}F fluoride. The line source was positioned at 0, 4, 8, 12, 16, and 20 mm away from the central axis of the scanner, respectively, and was parallel to the Y axis as defined in Fig. 3. Projection data were acquired using two detectors with a detector-to-detector distance of 220 mm. These projection data were reconstructed by both planar tomography and focal-plane reconstruction approaches. Three-dimensional reconstructed images with $36 \times 32 \times 58$ voxels were obtained by planar tomography, and two-dimensional projection images with 35×31 pixels were obtained by focal-plane reconstruction, with the focal plane defined at the center $(\mathrm{Z} = 0\ \mathrm{mm})$.

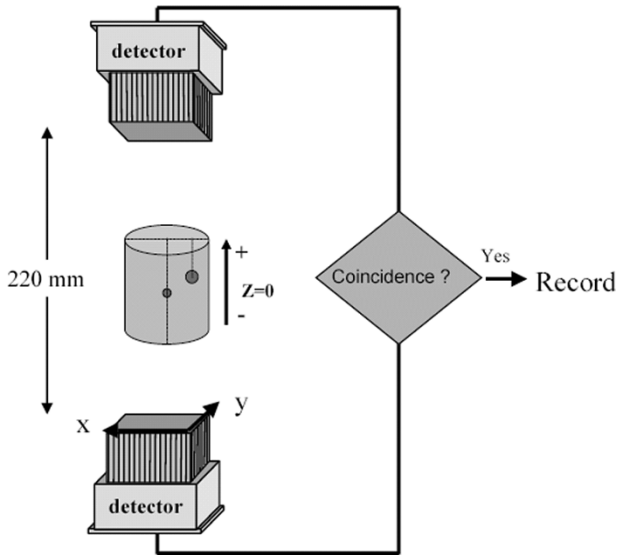

Fig. 3. Geometric set for scanning the breast phantom.

Profiles were drawn perpendicular to the reconstructed line images. Each FWHM was determined by linear interpolation.

The tomographic resolution was measured using the same line source. The source and its position for scanning were described as above. All data were obtained using full three-dimensional acquisitions with a rotating diameter of 220 mm. The detectors were rotated by 90° in steps of 3°. The scanning time was 120 sec per angle. Radial and tangential resolutions, which correspond to the X and Z directions in Fig. 3, were measured at 0, 4, 8, 12, 16, and 20 mm radial displacements from the central axis of the scanner. Data were reconstructed using filtered-backprojection with a ramp filter with a 0.7 cutoff at the Nyquist frequency. The radial and tangential FWHMs were obtained by linear interpolation from line profiles.

E. Phantom Studies

A water-filled cylinder with an interior diameter of 44.4 mm and a height of 82 mm was used to simulate a breast phantom. Five hollow spheres with diameters of 2 mm, 3 mm, 5 mm, 8 mm, and 10 mm were filled with radioactivity solution to simulate tumors in a breast (Fig. 4). Two separate, opposing detectors were used to scan the cylinder. The distance between the detectors was 220 mm. Fig. 3 displays the geometric setup used in the phantom study.

Initially, a single radiation source placed at various depths (Z direction) was measured. The cylinder was filled with water, and a 2 mm sphere with an radioactivity of around 0.02 mCi was placed at $\mathrm{Z} = -10\ \mathrm{mm}$, -20 mm, and -30 mm for scanning. The scan time for each measurement was 10 min. The maximum FWHMs of the hot spot were determined from the line profiles drawn on the reconstructed X-Y and Y-Z images using the linear interpolation. This experiment indicates the spatial dependence of the ability to detect tumors.

Five spheres with diameters of 2 mm, 3 mm, 5 mm, 8 mm, and 10 mm were inserted into the water-filled cylinder consecutively for scanning. All the spheres were placed at the center of the cylinder $(\mathrm{Z} = 0\ \mathrm{mm})$. The sizes of the sphere were estimated from the FWHMs of the hot spots in the reconstructed images.

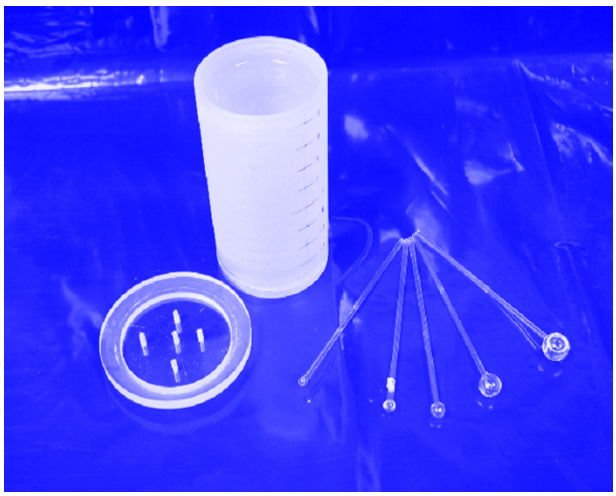

Fig. 4. Photograph of the cylindrical phantom (44.4 mm inner diameter × 82 mm height) and the hollow spheres. The interior diameters of the spheres are 2 mm, 3 mm, 5 mm, 8 mm, and 10 mm.

Two spheres placed at different depths in the cylinder phantom were used to verify the applicability of the PEImager to determine the hot-spot locations. A sphere with 2 mm size diameter was at the center of cylinder, and the other 3 mm sphere was 10 mm away from the center. Both of the two spheres were placed at the same depth $(\mathrm{Z} = 0\ \mathrm{mm})$ and were scanned for 10 min. In the following step, the 3 mm sphere was moved up to $\mathrm{Z} = +20\ \mathrm{mm}$ while the 2 mm sphere was kept at the same position, and another ten-minute scan was acquired. After data acquisitions, both the planar tomography and focal-plane reconstruction were used on the same data sets to reconstruct images.

The tumor-detection capacity power of planar tomography and focal-plane reconstruction were compared by resolving spheres surrounded by water with various tumor-to-normal tissue radioactivity ratios. Five spheres with diameters of 2 mm, 3 mm, 5 mm, 8 mm, and 10 mm were sunk to the center of the cylinder $(\mathrm{Z} = 0\ \mathrm{mm})$ one at a time for scanning. Both the cylinder and the hollowed spheres were filled with water with F-18 radioactivity. The tumor-to-normal tissue radioactivity ratios were set to 5:1, 10:1 and 20:1. The scan times were 5 min to 10 min to ensure the equality of the total counts for each scan. Planar tomography and focal-plane reconstruction were used to reconstruct the images following the serial scans.

All the list-mode data obtained by two-detector imaging were filtered with the low-energy threshold set to 430 keV and were binned to 82 944 LORs. Detector-efficiency calibration was applied before reconstruction. For planar tomography, ten iterations were used and the threshold value δ was $0.1 \times$ mean counts per voxel.

III. Results and Discussions

Fig. 5 shows the detector-efficiency response of each detector-element pair for the two typical opposite block detectors of the PEImager. The figure presents the 288 block images, and each block image has 288 pixels. The pixel value of each block image is the summed counts of a line of response after correction for the geometry factor. A flood source was measured to obtain these block images, so the detector efficiency response is assumed to be the only factor that influences the uniformity of the counts of LORs after geometric calibration. Therefore, the pixel values of the block images were used to normalize the detector efficiency.

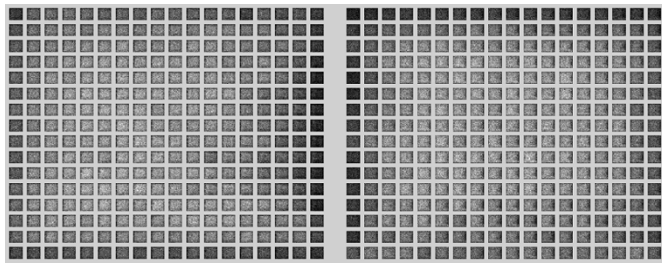

Fig. 5. Detector-efficiency response of each detector-element pair for two typical opposite block detectors of PEImager.

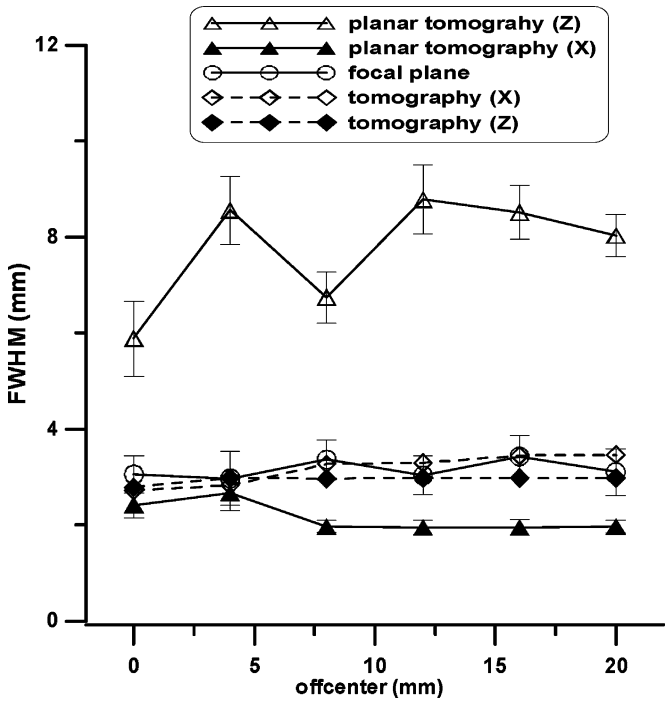

Fig. 6. Comparison of spatial resolution (FWHM) versus off-center distance relationships obtained by planar tomography, focal-plane tomography, and conventional tomography.

Fig. 6 compares the relationships between the spatial resolution (FWHM) and the off-center distance determined by planar tomography, focal-plane reconstruction and conventional tomography. White rhombus dots and dark rhombus dots represent the radial and tangential resolutions of conventional tomography, which correspond to the X and Z directions, respectively line. The transaxial resolution at the center is 2.73 mm in the X direction and 2.99 mm in the Z direction. The resolution in the X direction (radial) is worse (3.48 mm FWHM) at 20 mm away from the center, and the resolutions in the Z direction (tangential) are between 2.79 and 2.99 mm. The focal plane was defined at $\mathrm{Z} = 0\ \mathrm{mm}$ for focal-plane reconstruction; only one line (dark circles) represents the resolution in the X direction. The dark triangles plot the resolution of planar tomography in the X direction; white triangles represent the resolution

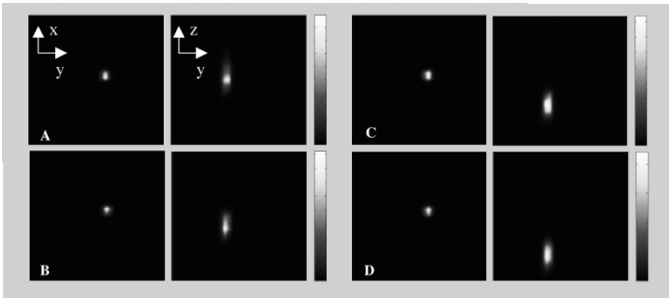

Fig. 7. An [^{18}F]-FDG solution filled 2 mm sphere was inserted into the water-filled cylinder and was placed at $Z = 0$ mm, $Z = -10$ mm, $Z = -20$ mm and $Z = -30$ mm. The left panels of (a), (b), (c), and (d) show the estimated activity distributions in the X-Y planes at $Z = 0$ mm, $Z = -10$ mm, $Z = -20$ mm and $Z = -30$ mm. The right panels (a), (b), (c), and (d) demonstrate the estimated activity distribution in Z-Y planes at $x = 28$ mm. The mean hot-spot size in the X and Y directions is 1.89 mm (FWHM). The mean hot-spot size in the Z directions is 6.02 mm (FWHM).

in the Z direction. The resolutions in the X direction do not differ significantly among the three reconstruction methods. The resolutions in the Z direction averaged 7.76 ± 1.17 mm for planar tomography and 2.95 ± 0.08 mm for conventional tomography. The mean FWHM of planar tomography was 2.63 times that of conventional tomography. The limited LORs gathered from the stationary planar scan caused blurring in the Z direction for planar tomography. The number of LORs associated with planar tomography with only one pair of detectors without rotation was used, was 1/60 that of conventional tomography with two pairs of detectors, rotated at 30 angles. Restated, planar tomography can use limited LORs effectively to obtain Z-direction information. Clearly, the planar tomography can yield almost as much three-dimensional information as classical tomography, but the acquisition of data is simpler and takes less scanning time. The ratio of the scan time using a stationary dual head and that using four heads in this case is 1:6.

Fig. 7 presents the imaging results obtained using a 2 mm inner diameter sphere placed in the water-filled cylindrical phantom at locations $Z = 0$ mm, -10 mm, -20 mm, and -30 mm. The left panels of Fig. 7(a)–(d) present the estimated radioactivity distributions of X-Y planes at $Z = 0$ mm, $Z = -10$ mm, $Z = -20$ mm and $Z = -30$ mm. The right panels of Fig. 7(a)–(d) present the estimated radioactivity distribution in the Z-Y planes at $X = 28$ mm. Fig. 7 reveals that planar tomography can reconstruct detailed radioactivity distributions in the Z direction, even when the hot sphere was not placed in the center $(Z = 0$ mm). The average mean hot-spot size along X and Y directions is 1.89 mm (FWHM), and the average hot-spot size in the Z directions is 6.02 mm (FWHM). Fig. 8 plots the estimated hot-spot sizes of the 2 mm sphere placed at various locations, and reveals that the estimated size of the hot spot is not significantly related to the locations of tumors. Five spheres with diameters of 2 mm, 3 mm, 5 mm, 8 mm, and 10 mm inserted in the center of a water-filled cylinder were scanned to measure the size of the tumor. The regression line in Fig. 9 plots the relationship between the spherical diameter and the hot spots' FWHMs determined from the reconstructed images. The experiments showed the feasibility of estimating the size of the tumor from the planar tomograms.

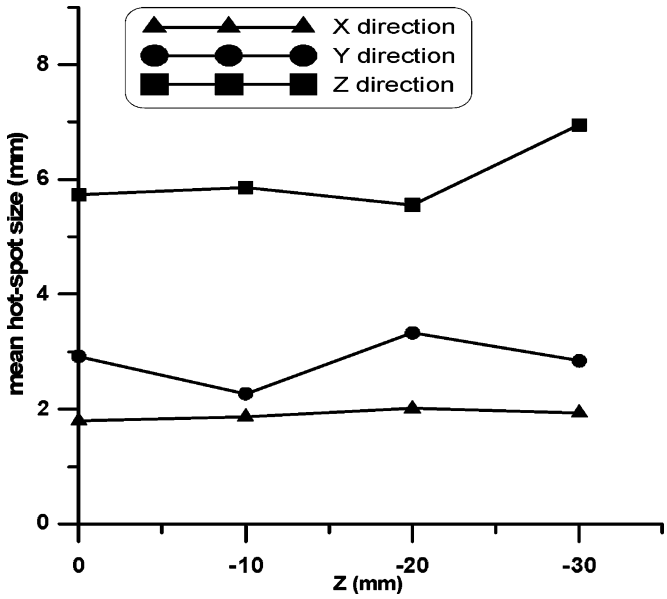

Fig. 8. Estimated hot-spot sizes of a 2 mm sphere placed at different locations for scanning.

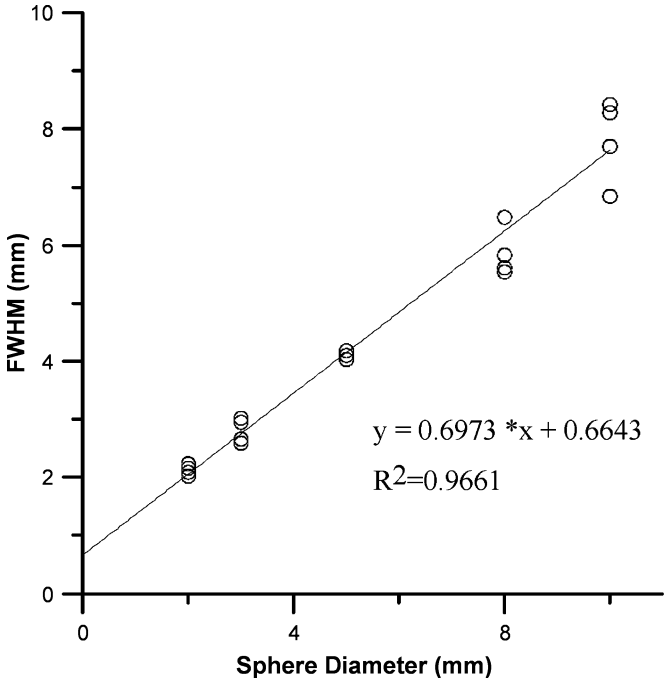

Fig. 9. Regression line between spherical diameter and hot spots' FWHM sizes determined from reconstructed images.

Fig. 10(a) presents the X-Y slices at $Z = +20$ mm and $Z = 0$ mm from focal-plane reconstruction and Fig. 10(b) presents images of the same slices obtained by planar tomography. In this case, the 2 mm and 3 mm spheres were positioned at $Z = 0$ mm and $Z = 20$ mm simultaneously for scanning. In Fig. 10(b), the smaller hot spot was most probably located at $Z = 0$ mm, and the larger one was most probably located at $Z = +20$ mm, as determined by planar tomography. The estimated results agree with the exact positions of the two spheres during the scan. Comparing Fig. 10(a) and 10(b) reveals that detecting the locations of the two spheres at various depths is

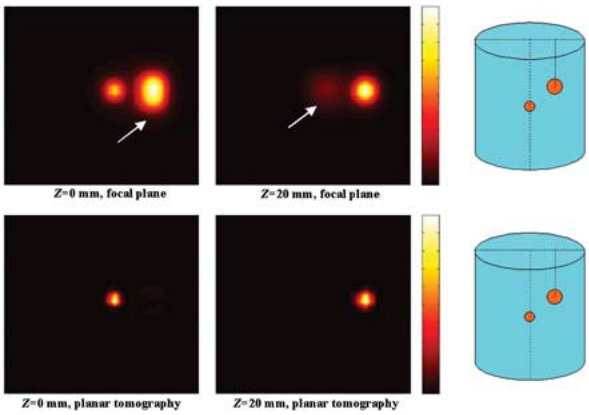

Fig. 10. A 2 mm [^{18}F]-FDG filled sphere at $Z = 0$ cm, and the other 3 mm sphere at $Z = +20$ mm were scanned simultaneously. Two X-Y plane images at $Z = 0$ mm and $Z = 20$ mm were shown. The top images were obtained from conventional focal-plane reconstruction, and the bottom images were obtained by planar tomography. The left and the right arrows indicate the shadows from the 3 mm and 2 mm spots, respectively. Clearly, the two spots were more easily inspected by planar tomography than conventional focal-plane method.

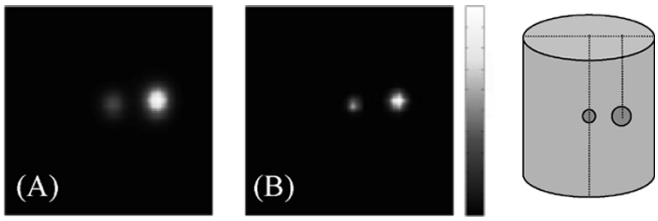

Fig. 11. 2 mm and 3 mm spheres filled with F-18 solution were placed in the water-filled cylinder at $Z = 0$ mm. The horizontal distance between the two spheres was 10 mm. This figure presents images of an X-Y slice, which were reconstructed by (a) focal-plane reconstruction, and (b) planar tomography.

more difficult using focal-plane reconstruction. The location of the lesion in the Z direction was estimated from slices with the most focused distribution of radioactivity for focal-plane reconstruction. A focused spot distribution might be mixed with other nonfocused distribution from other lesion, as in Fig. 10(a), if more than one hot spot are present at different Z depths. This raises difficulties in the interpretation of the multiple lesions. Fig. 11 also presents $Z = 0$ mm slice images Fig. 11(a) obtained by focal-plane reconstruction and Fig. 11(b) by planar tomography, when both the 2 mm and 3 mm spheres were placed at $Z = 0$ mm. Fig. 12 shows the two-spot profiles for comparison. It reveals that planar tomography better estimates the background radioactivity between the two hot spots, indicating that planar tomography has better contrast performance than the focal-plane reconstruction. The comparisons of planar tomography and focal-plane reconstruction show that the planar tomography performs better in determining the Z-direction locations of lesions and improves the image quality, regardless of whether the lesions were located at different, or the same, Z depths.

Fig. 13 displays the tumor-detection ability capability of planar tomography and focal-plane reconstruction. For the 80-mm-deep water phantom, the 3-mm-diameter tumor can be detected by applying planar tomography (bottom, right) with a 20:1 tumor-to-normal tissue radioactivity ratio, whereas the

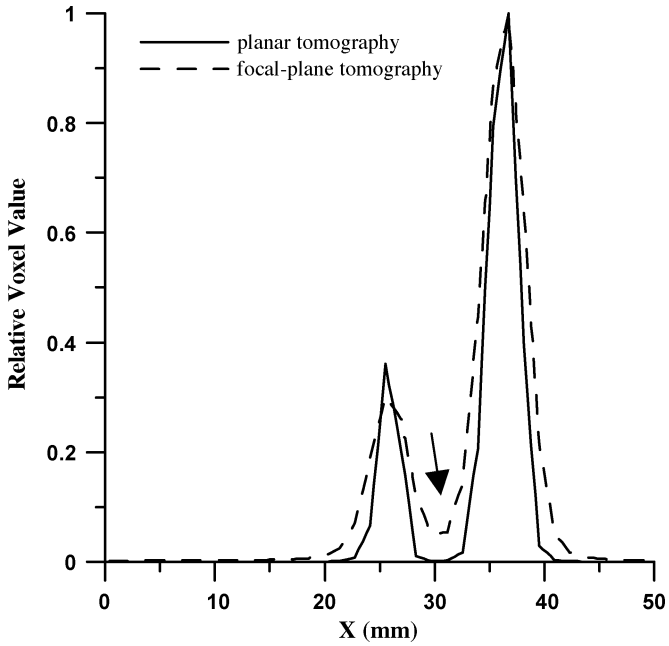

Fig. 12. Two-spot profiles were obtained from the images reconstructed by focal-plane and planar tomography. Planar tomography yields a more accurate estimate of the background radioactivity (arrow).

5-mm-diameter tumor (bottom, middle) and the 10-mm-diameter tumor (bottom, left) can be detected at ratios 10:1, and 5:1, respectively. The results obtained by the focal-plane method (middle) are shown for comparison. Neither planar tomography nor focal-plane reconstruction can identify the 2 mm tumor at ratios 20:1, 10:1, and 5:1. Results obtained by planar projection method, which was a common used in dual-head systems are displayed in top low of Fig. 13. The data show that planar tomography is the best among the three able to detect tumors. In this case, normal radioactive tissue was everywhere at a depth of 80 mm. The ratio of the size of the sphere to that of the phantom in the Z direction was small, and the solid angle comprised by LORs was limited. Although none of the circumstances favored planar tomography, the tumor-detection capacity of dual-head imaging with planar tomography was encouraging.

IV. Conclusion

This work showed the feasibility of using the PEImager in positron emission mammography studies. Although the PEImager comprises four position-sensitive imaging blocks for detection, only two opposing detectors were employed to implement the work of PEM to reduce the cost of constructing a dedicated scanner for breast cancer in the future. The detectors were stationary during data acquisition, so planar tomography was used to reconstruct 3D image from limited LORs. A noise-cut threshold method was used during reconstruction to increase the signal-to-noise ratio and the rate of convergence. Spatial resolutions of planar tomography, focal-plane reconstruction and conventional tomography were compared. Planar tomography can exploit the limited LORs to yield Z-direction information, although the blurring in the Z direction is approximately three

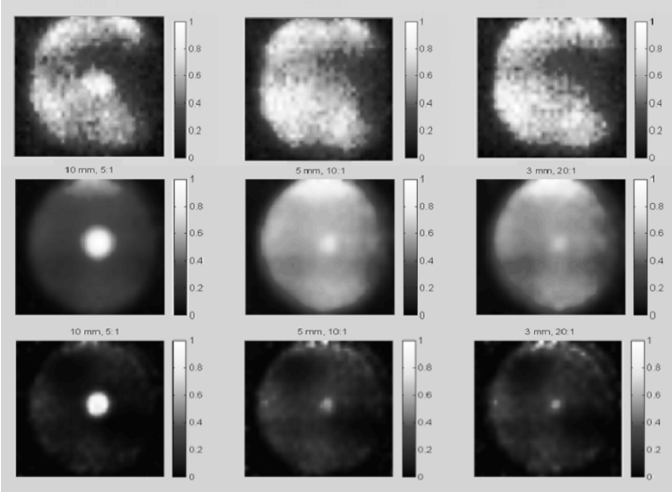

Fig. 13. For an 80-mm-deep phantom with a 20:1 tumor-to-normal tissue radioactivity ratio, the 3-mm-diameter tumor can be detected by planar tomography (bottom, right). The 5-mm-diameter tumor (bottom, middle) and the 10-mm-diameter tumor (bottom, left) can be detected at ratios of 10:1 and 5:1, respectively. The planar tomography is better able to detect tumors than is the conventional focal-plane method (middle row). The results of planar projection method (top row) were presented for references.

times that of conventional tomography given the current geometric setting. The locations and sizes of the hot spot can be estimated from the final reconstructed images, and the estimate has no significant spatial relationship with the locations and sizes of hot spot. When the planar tomography described here was used, the minimum lesion detectable sizes were 3 mm, 5 mm, and 10 mm with tumor-to-normal tissue radioactivity ratios of 20:1, 10:1, and 5:1, respectively. The pilot study shows the potential of PEM with dual-head imaging. A dedicated PEM scanner with a large detective area and flexible gantry to gather more information from limited LORs will be expected to provide a simple, effective and inexpensive way for early detection of breast cancers.

ACKNOWLEDGMENT

The authors would like to acknowledge C.-S. Shyu (Physics Division, INER) for manufacturing phantoms and handling positron sources, Dr. W.-J. Lin and J.-T. Chen (Isotope Applications Division, INER) for providing F-18-fluoride.

REFERENCES

[1] R. Freifelder and J. S. Karp, "Dedicated PET scanners for breast imaging," *Phys. Med. Biol.*, vol. 42, pp. 2463–2480, 1997.

[2] L. P. Adler, P. F. Faulhaber, and K. C. Schnur *et al.*, "Axillary lymph node metastases: screening with [F-18]2-deoxy-2-fluoro-D-glucose (FDG) PET," *Radiology*, vol. 203, pp. 323–327, 1997.

[3] J. P. Crowe, L. P. Adler, and R. R. Shenk *et al.*, "Positron emission tomography and breast masses-comparison with clinical, mammographic, and pathological findings," *Ann. Surgical Oncology*, vol. 1, pp. 132–140, 1994.

[4] K. F. Hubner, G. T. Smith, and J. A. Thie *et al.*, "The potential of F-18-FDG PET in breast cancer. Detection of primary lesions, axillary lymph node metastases, or distant metastases," *Clinical Positron Imaging*, vol. 3, pp. 197–205, 2000.

[5] C. J. Thompson, K. Murthy, and I. N. Weinberg *et al.*, "Feasibility study for positron emission mammography," *Med. Phys.*, vol. 21, pp. 529–538, 1994.

[6] W. W. Moses, T. F. Budinger, and R. H. Huesman *et al.*, "PET camera designs for imaging breast cancer and axillary node involvement," *J. Nucl. Med.*, vol. 36, p. 69P, 1995.

[7] I. Weinberg, S. Majewski, and A. Weisenberger *et al.*, "Preliminary results for positron emission mammography—real-time functional breast imaging in a conventional mammography gantry," *Eur. J. Nucl. Med.*, vol. 23, pp. 804–806, 1996.

[8] N. K. Doshi, Y. P. Shao, and R. W. Silverman *et al.*, "Design and evaluation of an LSO PET detector for breast cancer imaging," *Med. Phys.*, vol. 27, pp. 1535–1543, 2000.

[9] K. Murthy, M. Aznar, and A. M. Bergman *et al.*, "Positron emission mammographic instrument: initial results," *Radiology*, vol. 215, pp. 280–285, 2000.

[10] R. R. Raylman, S. Majewski, and R. Wojcik *et al.*, "The potential role of positron emission mammography for detection of breast cancer. A phantom study," *Med. Phys.*, vol. 27, pp. 1943–1954, 2000.

[11] M. L. Jan, H. C. Liang, and S. W. Huang *et al.*, "Preliminary results from the AROPET," in *Proc. 2001 IEEE Nuclear Science Symp. and Medical Imaging Conf.*, San Diego, CA, pp. 1607–1610.

[12] H. Uchida, T. Okamoto, and T. Ohmura *et al.*, "A compact planar positron imaging system," *Nucl. Instrum. Methods Phys Res. A*, vol. 516, pp. 564–574, 2004.

[13] G. Muehllehner, M. P. Buchin, and J. H. Dudek, "Performance parameters of a positron imaging camera," *IEEE Trans. Nucl. Sci.*, vol. 23, pp. 528–537, 1976.

[14] G. F. Knoll, *Radiation Detection and Measurement*, 3rd ed. New York: Wiley, 2000.

[15] J. S. Huber, S. E. Derenzo, J. Qi, W. W. Moses, R. H. Huesman, and T. F. Budinger, "Conceptual design of a compact positron tomograph for prostate imaging," *IEEE Trans. Nucl. Sci.*, vol. 48, no. 4, pp. 1506–1511, Aug. 2001.

[16] C. M. Kao and C. T. Chen, "Development and evaluation of a PET system for high-throughput small-animal imaging," in *Proc. 2003 IEEE Nuclear Science Symp. and Medical Imaging Conf.*, Portland, OR.

[17] L. A. Shepp and Y. Vardi, "Maximum likelihood reconstruction for emission tomography," *IEEE Trans. Med. Imag.*, vol. MI-1, pp. 113–122, 1982.

[18] Y. Vardi, L. A. Shepp, and L. A. Kaufman, "Statistical model for positron emission tomography," *J. Amer. Stat. Assoc.*, vol. 80, pp. 8–20, 1985.

[19] K. S. Chuang, M. L. Jan, J. Wu, S. Chen, Y. C. Ni, and Y. K. Fu, "The thresholding MLEM algorithm," *J. Med. Biol. Eng.*, vol. 24, pp. 85–91, 2004.